Analysis of Origami Flasher-Inspired Deployable Structures Through Dynamic and Experimental Modeling

by

Jane Bai

Submitted to the Department of Mechanical Engineering in partial fulfillment of the requirements for the degree of

BACHELOR OF SCIENCE IN MECHANICAL ENGINEERING

at the

MASSACHUSETTS INSTITUTE OF TECHNOLOGY

May 2024

Authored by:

Jane Bai
Department of Mechanical Engineering
May 2024

Certified by:

Maria Yang
Associate Dean of Engineering
Thesis Supervisor

Accepted by:

Ken Kamrin
Professor of Mechanical Engineering & Applied Mathematics
Undergraduate Officer

Analysis of Origami Flasher-Inspired Deployable Structures Through Dynamic and Experimental Modeling

by

Jane Bai

Submitted to the Department of Mechanical Engineering in May 2024, in partial fulfillment of the requirements for the degree of

BACHELOR OF SCIENCE IN MECHANICAL ENGINEERING

Abstract

The Origami “flasher” model holds immense engineering promise due to its ability to alternate between a compressed 3-dimensional form and a deployed 2-dimensional form. While zero-thickness mathematical models have been thoroughly covered, dynamic modeling and material exploration are essential for the successful design of finite-thickness models. In this research, the mathematical effects of parameters such as center polygon size, unit panel length, and crease arrangement on flasher surface area optimization are first established. Software is then used to create a dynamic model that combines kinematic analysis with material properties to visualize the folding geometry and internal strain of the flasher pattern and to identify points of analysis for the experimental model. Finally, a stored-energy-based deployable experimental model is made using Yupo paper and video analysis done to understand damping behavior, deployment trajectory, and torque distribution. A discussion on design considerations for flasher patterns follows and potential topics for future research are set forth.

Thesis Supervisor: Maria Yang
Title: Associate Dean of Engineering

Acknowledgements

I first want to thank my thesis advisor Professor Maria Yang for her encouragement, patience, and support throughout the research and writing process. I am also indebted to Barbara Hughey and the 2.670 laboratory for loaning me measurement instrumentation and to Coby Unger, Hayami Arakawa and the staff of N51-120 for their guidance and machine training. Finally, I am grateful for Dr. Yi Zhu of the Department of Civil and Environmental Engineering at the University of Michigan and to Amanda Ghassaei in their assistance for the development of the dynamic model within my research.

Contents

List of Figures

List of Tables

Introduction

Origami-based deployable designs are used and researched within engineering for the creation of structures that can change between a compact and larger, unfolded form. By exploring the behavior of and principles behind these deployable origami patterns, engineers can develop innovative products and technologies for practical real-world use. Applications of deployable origami range from the astronomical to submicroscopic level: it serves as the basis for JPL's StarShade, an occulter for the future New World's mission, and Zhang et. al [1] demonstrated its promise within the biomedical field regarding antibody specificity and performance. Mathematical modeling has led to better understanding of deployable origami mechanics but research into real-life adaptations is becoming more important regarding future engineering practices.

The Origami "flasher" pattern is similar to more well-known patterns such as the Miura-ori and square-twist methods and is a foldable template that utilizes alternations of mountain and valley creases to create dynamic synchronous folding action. Shafer and Palmer [2] are credited with naming and developing flasher models whose geometric properties and folding mechanics can easily be studied through planar-graph concepts. Their approach provided a systematic framework for studying the flasher model and contributed to a better understanding of its design principles. Figure 1.1 shows the original square-based flasher pattern set forth by Shafer and Palmer.

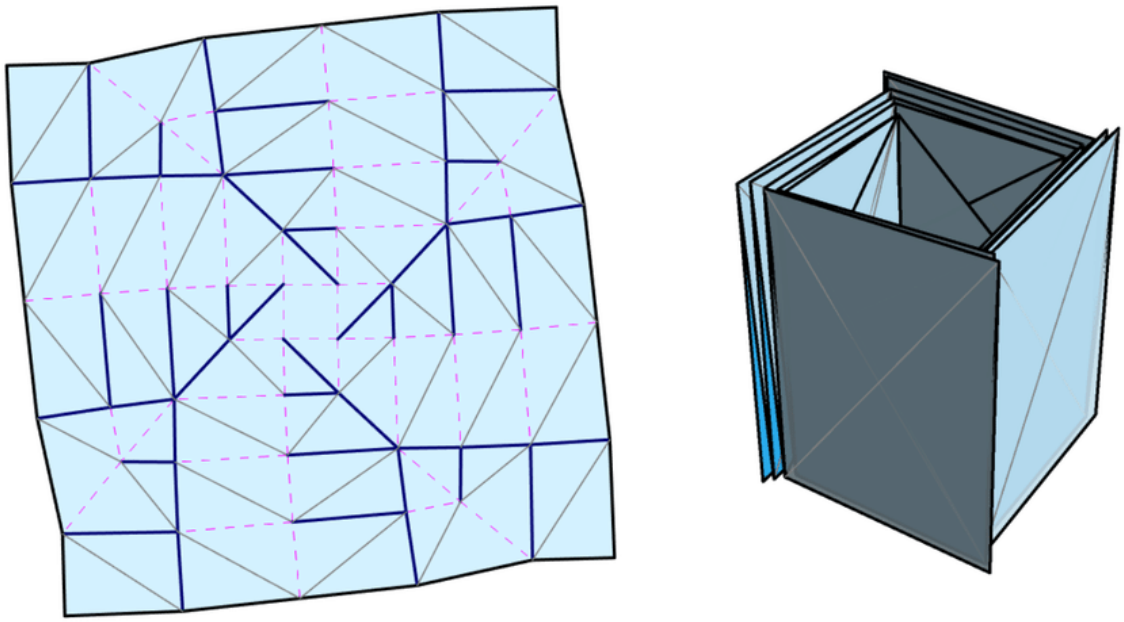

Figure 1.1. Shafer and Palmer's original "flasher" model.

A flasher consists of a central polygon whose edges connect to extending panels, each with identical crease geometry. The valley folds of the subunits primarily dictate the main axes along which the flasher will fold, while the mountain folds control aspects such as the size of subunits within each panel and angles of deployment. When "deployed", all panels and subunits of the pattern are visible, and the model is entirely 2-dimensional. When "compressed", the flasher becomes 3-dimensional, and its surface area decreases as the crease geometry allows for exposure only of the outermost subunits of the panels.

The models developed by Shafer and Palmer do not account for material effects and are thus "zero-thickness" models. Research into developing "finite-thickness" models aims to either reduce the effect of material constraints on the model, or to introduce new mechanisms that allow for the zero-thickness model to still be accurate. Hoberman [3]

demonstrated the effectiveness of adding hinge mechanisms along flasher folds to encourage flexibility rather than relying solely on crease geometry. Trautz and Kunstler's research [4] explored constraints that material stiffness imposes on flasher deployment and recommend that elastic materials be used due to their reduction of load-bearing capacity through the ability to conform to more complex patterns. Tachi et al. [5] demonstrated that introducing finite thickness between coplanar facets allows for performance like that of a non-zero thickness model.

To minimize the problems arising from finite-thickness models, elastic material can be beneficial for modeling flasher geometry regarding future products. For example: polycrystalline silicon and ethylene tetrafluoroethylene (ETFE) are materials used in flexible photovoltaic structures that have begun to populate the consumer market. Yupo paper is an ideal medium for experimental exploration due to its dynamic properties. Made from 3 bi-axial layers of polypropylene resin in a patented manufacturing process, it is extremely tear-resistant. Its lamination prevents dust accumulation and adds to its durability when folded, stretched, or bent.

The first section sets the mathematical basis for the experimental model by establishing a mathematical relationship between flasher geometric parameters and deployment ratio. Next, dynamic-modeling software is used to identify design concerns and constraints. Finally, data analysis on an experimental model is made from the novel material Yupo gives rise to a discussion on flasher geometry performance and its future applications.

Mathematical Model

Shafer and Palmer's original 1995 model is simplistic and uses squares as the center polygon and extending panels. While effective in ensuring isometry within the folded 3-dimensional form, it is not optimized for surface area deployment or ease. However, it is useful as a base for developing more effective models.

The flasher pattern for this research consists of a center polygon encircled by an array of identical panels with creases. Blue corresponds to a valley fold, red to a mountain fold, and black for a boundary edge. When folded, each of the panels partially wrap around the center polygon and are layered on top of one another: forming an open-ended cylinder whose base is defined by the center polygon and height by the geometric shape of the subunits within the panels.

The number of sides of the center polygon, also known as the order of the flasher, is denoted by n, and the length of each of its sides, a. Each panel extending from the center polygon forms a rectangular "kite" shape with the primary vertex angle denoted as θ. The panels are further divided into subunits. The panels are first bisected diagonally lengthwise by a mountain crease, and each half then further divided depending on a parameter we will call height: h. This height parameter also defines the number of times the panel's diagonal mountain crease wraps around the center polygon when the flasher is in its folded form. Figure 2.1 shows flashers of varying order.

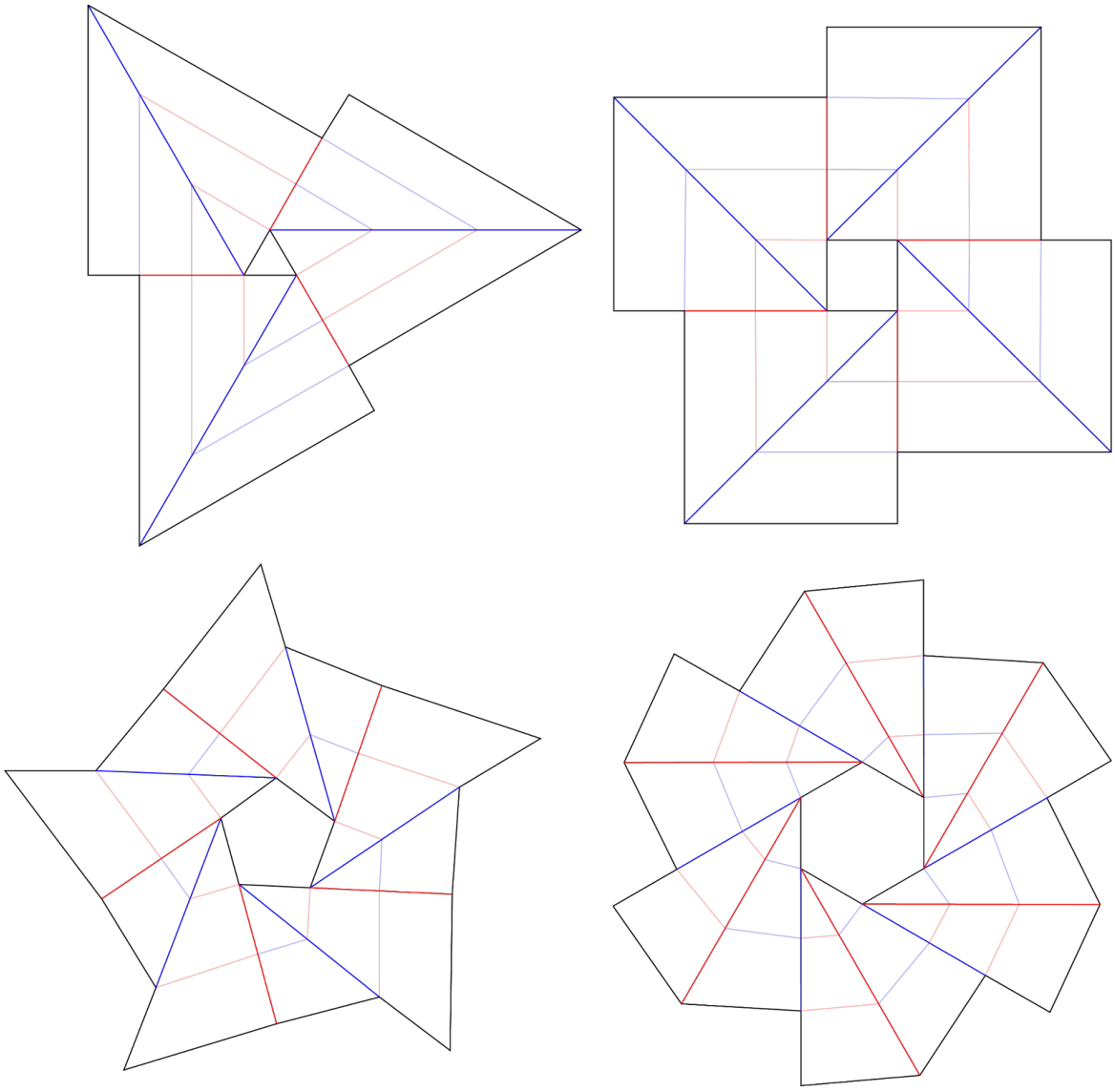

Figure 2.1. Clockwise from top left, flashers of $n = 3, 4, 5, 6$.

For design and analysis simplicity, we impose further constraints when creating flasher patterns:

- The non-vertex angles of the panels are always 90 degrees.
- $h = 3$.
- The outer length of each panel's subunits is equivalent to a.

These constraints allow for radial symmetry within the flasher and greatly simplify analysis. As each panel is identical, it is sufficient to isolate one for data collection and construct a model of the full flasher through it.

The flasher pattern's ability to change between its compact 3-dimensional form and larger 2-dimensional deployed form can be quantified using the parameter $R_{Deployment}$, which represents the ratio of the flasher pattern's surface area when unfolded to folded. The unfolded flasher has all subunits of each panel exposed and the total area is therefore the area of the center polygon and all subunits. When folded, only one of each panel's outermost subunits is exposed. Thus, the folded area depends only on the area of the center polygon and the area of the last subunit. With this knowledge, it is straightforward to calculate $R_{Deployment}$ in terms of n, h, a as shown in equations 1-4.

$$R_{Deployment} = \frac{A_{Center\ Polygon} + \sum A_{Subunits}}{A_{Center\ Polygon} + A_{Subunit,\ h}} \qquad (1)$$

$$A_{Center\ Polygon} = \frac{na^2}{4\tan\frac{\pi}{n}} \qquad (2)$$

$$\sum A_{Subunits} = nha^2 \tan\frac{\pi}{n} \qquad (3)$$

$$A_{subunit,\ h} = \frac{1}{2}a^2 \tan\frac{\pi}{n}(2h-1) \qquad (4)$$

The lowest possible order for a flasher is 3 and results in a triangular flasher pattern. There is no theoretical limit to a flasher's order, for as it approaches infinity, the center polygon takes a circular form and the 3-dimensional shape becomes cylindrical and $R_{Deployment}$ approaches a stable value, as shown in Figure 2.2.

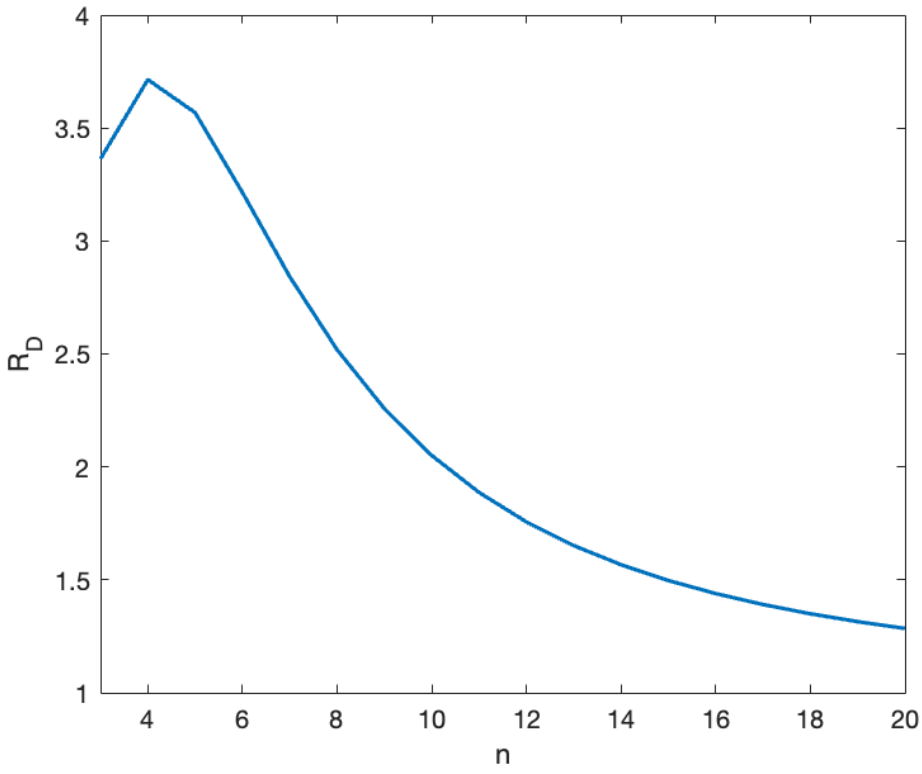

Figure 2.2. $R_{Deployment}\ vs. n.$

The original flasher model proposed by Shafer and Palmer has an order of 4 and with the highest $R_{Deployment}$, seems to be the optimized choice. However, this square deployment model has already been extensively studied. While an order of 5 resulted in the next largest $R_{Deployment}$, its use within models is complicated by the fact that flashers of an odd order result in polygons without point symmetry and imperfect tessellation. While not a problem for a dynamic model created by software, it complicates the creation and deployment of an experimental model. A flasher of order 3 also has a large $R_{Deployment}$, but as seen in Figure 2.1, the proportions of the subunits within its panels pose considerable design obstacles.

As the chosen model will serve as the template for an experimental model, mechanical factors such as the torque experienced by joints located at creases are important. Bhuiyan [6] demonstrated that as order increases with the surface area of the entire model held constant, the maximum force experienced by a panel decreases. This assumption means that a flasher of order 6 emerges as the ideal choice due to its large $R_{Deployment}$ of 3.214, rotational and point-wise symmetry, and a potential to limit detrimental mechanical effects. Figure 2.3 shows the center polygon and one panel of the n=6, h=3 pattern that serves as the basis for the dynamic and experimental model.

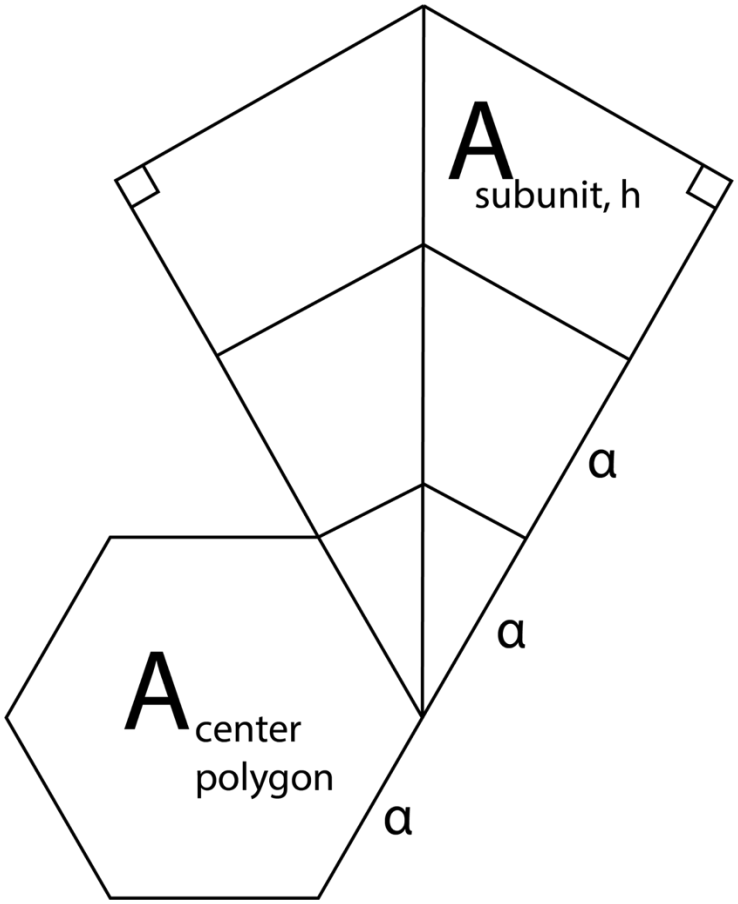

Figure 2.3. The center polygon & one panel of $n = 6, h = 3$.

Dynamic Model

In their design of a deployable solar-array, Zirbel et al. [7] isolated two effective ways to account for the internal strain felt due to material flexing during deployment. The first option is to further subdivide each panel's subunits with its own diagonal bisector: which we will call "facet creases". The greatest weakness of this model is that it is over-constrained, unstable, and therefore unsuitable for data analysis. The Grubler-Kutzbach [8] formula for spatial mechanisms can be used where F represents the degrees of freedom, N the total number of rigid links, j the number of joints, and f_j the degree of freedom for a joint j. As all hinges in a spherical linkage have 1 degree of freedom, $f_j = j$ and the formula can be further simplified into equation 5.

$$F = 3(N - 1 - j) + \sum_{i=1}^{j} f = \sum_{i=1}^{j} f - 3 \quad (5)$$

For our flasher pattern of $n = 6, h = 3$ as seen in Figure 3.1, we have 42 joints (including the center polygon) and thus the Grubler-Kutzbach formula shows that the model has 39 degrees of freedom. An experimental model was made incorporating these facet creases as true mountain and valley folds. While introducing these additional creases allowed for easier model deployment, they caused the model to be extremely stable as it became more prone to roll and pitch. As the experimental model relies on the stored energy of torsional strains for automatic deployment, roll and pitch would complicate analysis and therefore this approach was abandoned.

Zirbel et al.'s second approach was to add a thin "membrane" between panels joined by valley folds. They found this decreased the degrees of freedom for the model and that the optimal spacing between two panels was $2t$, with t equal to the thickness of the panels. This "expanded" model is shown on the right in Figure 3.1.

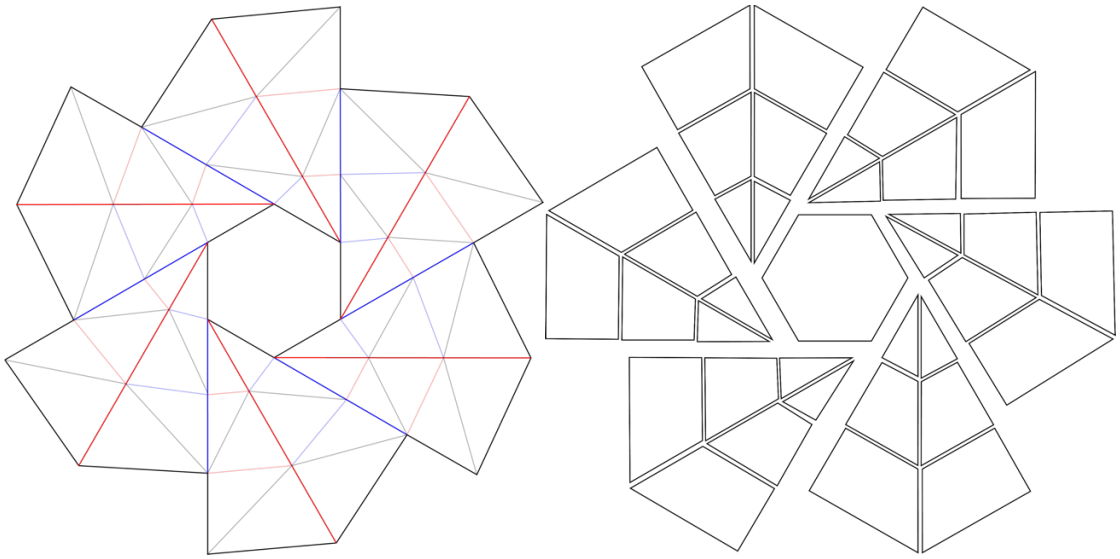

Figure 3.1. The over-constrained model with facet creases (left) and the expanded model with $2t$ spacing between subunits (right).

This second approach greatly reduces the model's degrees of freedom, but by excluding the diagonal bisectors within each panel's subunits, adds potential for the strain experienced at those locations to influence model behavior. To facilitate design and understand the behavior of an experimental model, it is necessary to create a dynamic model to aid in investigating strain and other mechanical properties. For this purpose, software was used.

If the flasher pattern is modeled as a truss-bar system, kinematic analysis is relatively straightforward through linear equations relating the internal tensions and

displacement of each subunit. However, the use of Yupo paper as a medium and the finite-thickness of our model means that material properties are not to be ignored. Schenk and Guest's structural engineering approach for modeling Miura folds [9] was extremely useful for this purpose. They were novel in their methodology as it allows for material properties to be introduced into the kinematic analysis via a "stiffness matrix". The linear algebra behind their method will not be included but a quick explanation of the stiffness factors is covered.

The most dominant factors found were axial stiffness and facet stiffness. Axial stiffness affects the distance constraints for the kinematic analysis, which in turn dictates how much each panel will stretch/compress (in short, deform) during deployment. The formula for axial stiffness relies on the area of the panel, Young's Modulus of the material, and the characteristic length along the axis of applied force. For our chosen flasher pattern, the force experienced within each panel is transverse and the Young's Modulus value of Yupo paper in the cross-direction is to be used. The characteristic lengths are taken as the facet creases as shown in Figure 3.1.

Facet stiffness represents the flexibility of the material within each subunit. As it increases, each subunit becomes more "rigid" and flattened against its creases. As Schenk and Guest treated the panels of Miura folds as truss bars, they defined the facet stiffness as the bending stiffness along facet creases. Our flasher pattern contains panels larger than typically found in Miura folds, so a different approach was used. Each subunit can be modeled as an internal joint with a hinge mechanism, called "intra-joint" for short, as shown in Figure 3.2. From this, we can apply beam bending theory to quantify the facet stiffness. Like axial stiffness, its formula depends on the cross-direction Young's Modulus

but differs in that we take the assumption that $L = 2t$ and use I, the moment of inertia for the hinge mechanism. Equations 6-7 are used to find the axial stiffness, K_A, and facet stiffness, K_F, for each panel.

$$K_A = \frac{EA}{L_c} \qquad (6)$$

$$K_F = \frac{EI}{L_c} = \frac{Ebt^3}{12 \times 2t} = \frac{Ebt^2}{24} \qquad (7)$$

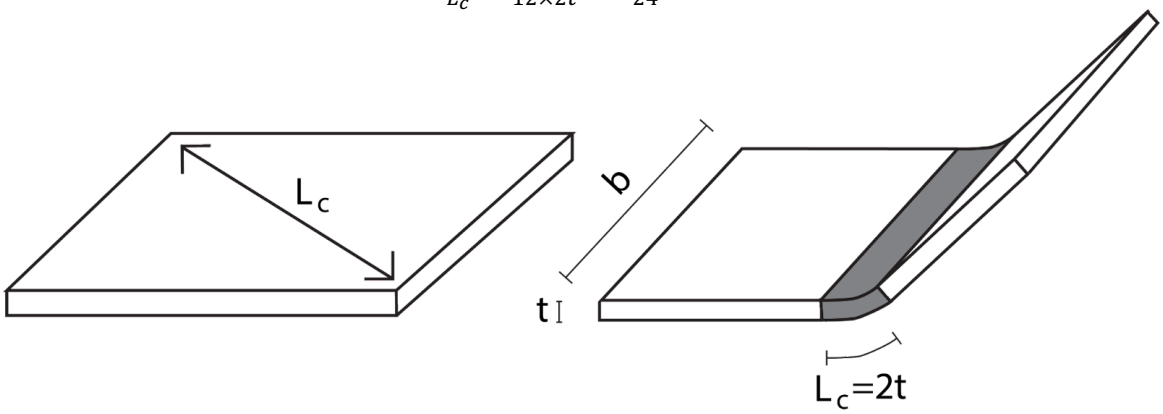

Figure 3.2. The "intra-joint": a subunit modeled as an internal hinge.

Lastly, the damping factor, which encapsulates rebound effects that arise due to material properties, must be quantified. Modeling each panel as an intra-panel hinge allows for us to use the facet stiffness to find the damping coefficient, given by equation 8. ζ represents the damping ratio, which can be approximated to be 0.08 using the value found experimentally by NASA [10] for 0.0075" thick Mylar in oscillating baffles with a minimal period parameter.

$$c = 2\zeta\sqrt{K_f I} = 1.92\sqrt{\frac{Eb^2t^5}{2}} \qquad (8)$$

Building on Schenk and Guest's work, Troise et. al [11] showed that iterative solving of the displacement constraint equilibrium for each component of a flasher model

was adequate for predicting its overall mechanical behavior, regardless of its number of degrees of freedom, meaning any software with finite-element-analysis capabilities is suitable. Additionally, the only boundary condition necessary is a cube along the three axes with dimensions correlated to the flasher deployed form. Finally, loading is defined as displacement constraints on the 6 outer-most vertices of each panel using the diagonal bisector as the axis of application.

Using the calculated values of K_A, K_F and c for our flasher of $n = 6, h = 3$, a dynamic model was built using MATLAB FEA and open-source code developed by Zhu et al. for origami simulation [12].

For internal strain visualization, the model was uploaded to an open-access website [13] designed to visualize 2-dimensional internal Cauchy strain for a given origami structure. Figure 3.3 shows the flasher at various deployment stages with green representing areas of high strain.

It is evident that in the absence of facet creases, the strain felt within the outermost panels is non-negligible and concentrated at the intra-joints. Additional strain is also concentrated at the locations of the mountain folds (the diagonal bisectors for each panel). These are areas where the experimental model experiences the largest deformations and forces during deployment. They represent an "inter-joint" between two subunits within a panel and were chosen for analysis via the experimental model.

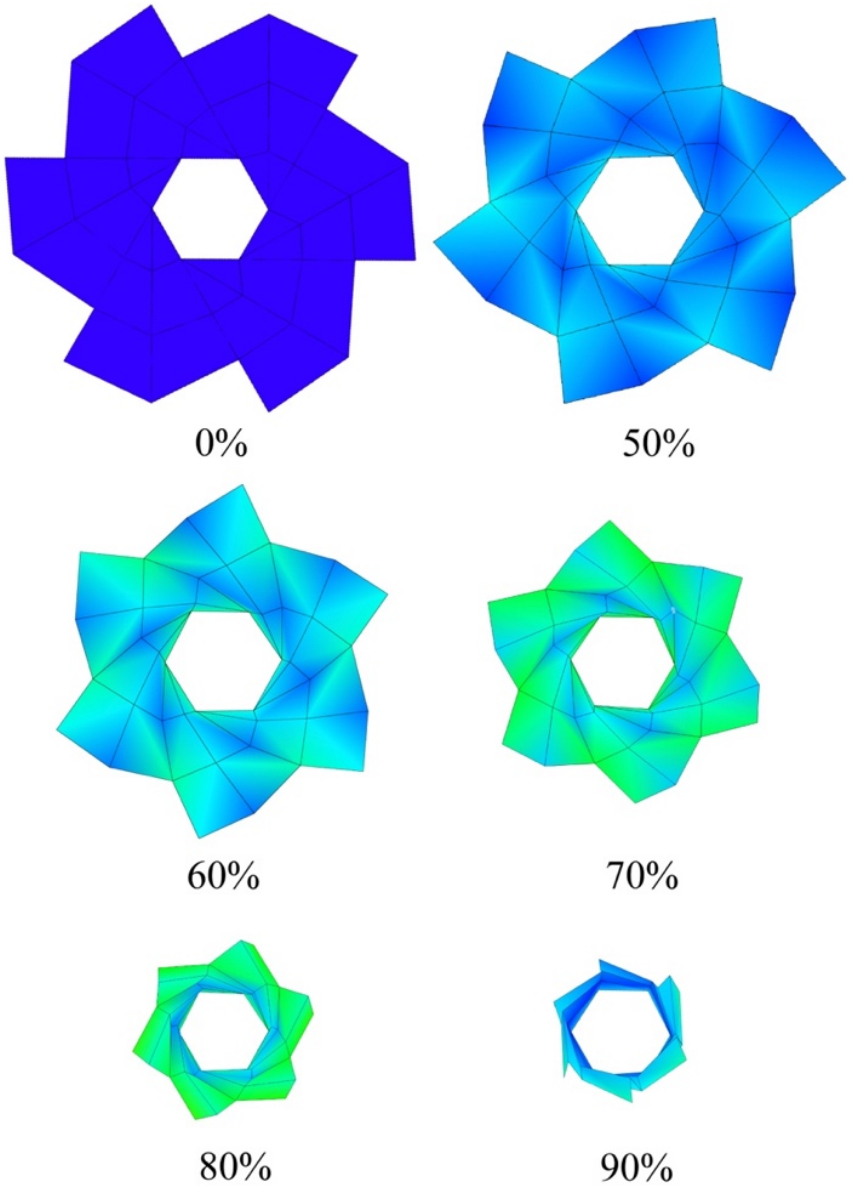

Figure 3.3. Strain distribution of a $n = 6, h = 3$ flasher.

The creation of this dynamic model which combines kinematic analysis along with material properties allows for comprehensive analysis of any similar flasher pattern. Figure 3.4 provides an example of flashers of order $n = 3, 4, 5$ at various stages of deployment imported into the software for strain analysis. By changing the values of K_A, K_F and c or

introducing different parameters, this dynamic model may be useful for examining flasher behavior across different materials and patterns.

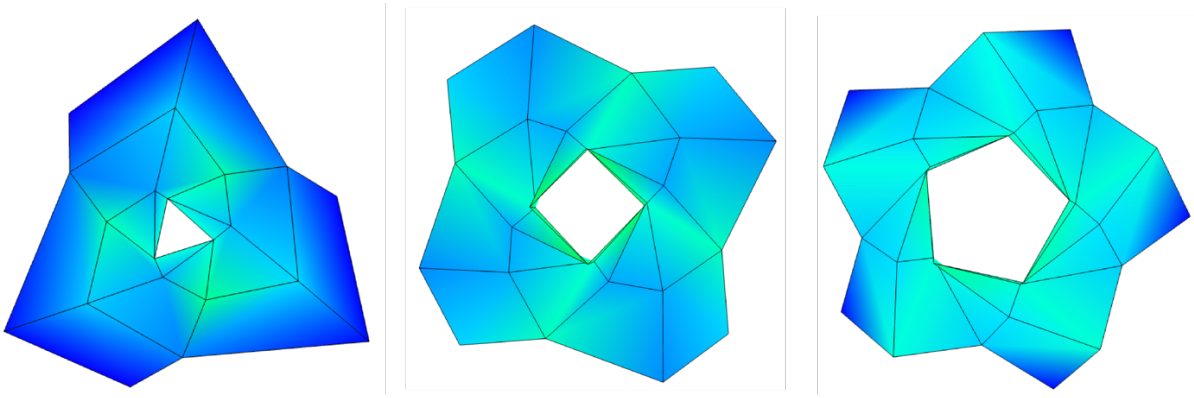

Figure 3.4. Strain distribution for flashers of $n = 3, 4, 5, h = 3$.

Experimental Model

The creation of an experimental model serves a dual purpose to validate the dynamic model and its parameters of concern and provides insight into potential design obstacles. Table 4-1 below lists the known material properties of 200 gsm Yupo, the material used as a basis for the experimental model.

Table 4-1. Material properties of Yupo.

	Thickness (μm)	Density ($\frac{g}{cm^3}$)	Elongation (%)	Tensile Strength ($\frac{kN}{m}$)	E (MPa)
Cross Direction	250	0.8	30	35	1372.9
Machine Direction	250	0.8	160	10	882.6

A $n = 6, h = 3$ flasher pattern with $a = 0.0557\ m$ was uploaded to an Epilog Fusion Edge 12 machine to cut a 20" x 26" Yupo sheet into the center polygon and subunits. Using Zirbel et al.'s recommendation on the use of thin membranes, clear Gorilla duct tape (made of polyethylene with acrylic adhesive) was used to connect subunits with gaps approximated to be around 0.0005 meters. To provide stability and reinforce the model's center of mass for easier data analysis, a replica of the center polygon was cut from 3mm thick acrylic and attached using tape.

Flasher-based models rely on a form of stored energy for automatic deployment. Within this model, torsional springs made of 302 stainless steel wire with an outer diameter of 0.302" and leg lengths of 1.25" are used for this purpose. To maximize deployment

effectiveness, they were placed at the mountain folds of each panel's outermost subunits and reinforced with tape. The torsional spring's legs create an angle of 180° when neutral and when the flasher is fully compressed, hold maximum potential energy as the angle is reduced to 0°. Through trial and error, it was found that introducing more springs at the lower mountain folds of each panel was unnecessary for automatic deployment and introduced more instability to the model.

By first calculating the spring constant, K_{Spring} of each torsional spring, the total potential energy stored in the compressed flasher can be found as shown in equations 9-11 [14]. *d* represents the wire diameter, E the elastic modulus of 302 stainless steel, *D* the mean spring diameter, and *N* the number of active coils. In addition to the potential energy and spring constant, the damping coefficient c can also be found by treating the spring as an inverted pendulum in Figure 4.1 with the mass of attached panels treated as point masses situated midway along each spring leg. We assume that $\zeta = 0.01$ for metals within the elastic deformation range and that when the flasher is folded, each spring reaches $\theta_{max} = \pi$. K_{Spring} has already been calculated, leaving only *I* to be found through implementing the mass of each outer subunit.

$$K_{Spring} = \frac{d^4 E}{64DN} = 0.042476 \ \frac{Nm}{rad} \qquad (9)$$

$$U_{total} = 6 \times \left(\frac{1}{2} K_{Spring} \theta_{max}^2\right) = 1.25766 \ N \qquad (10)$$

$$c = 2\zeta\sqrt{K_{Spring} I} = 1.93871 \times 10^{-7} \qquad (11)$$

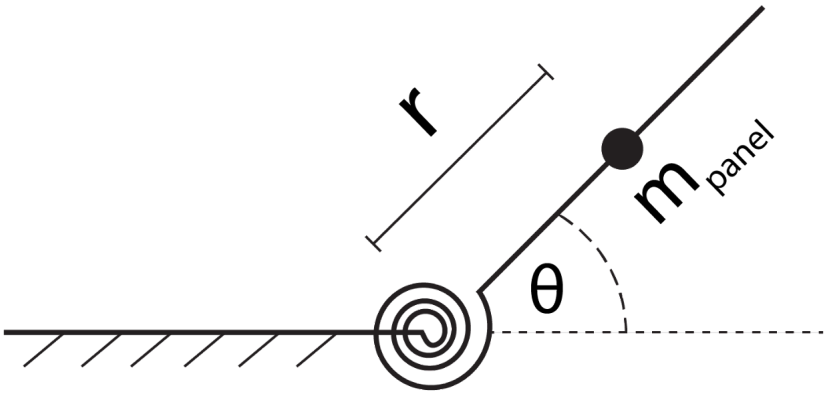

Figure 4.1. The torsional spring as an inverted pendulum.

To limit frictional effects, acrylic plexiglass served as the surface for deployment and was painted black to maximize contrast for video analysis purposes. A camera placed at a distance of 1.2 m above the center of the flasher recorded the deployment process for video analysis. Figure 4.2 shows the flasher model after assembly in its fully deployed and compressed forms and with joints chosen for video analysis.

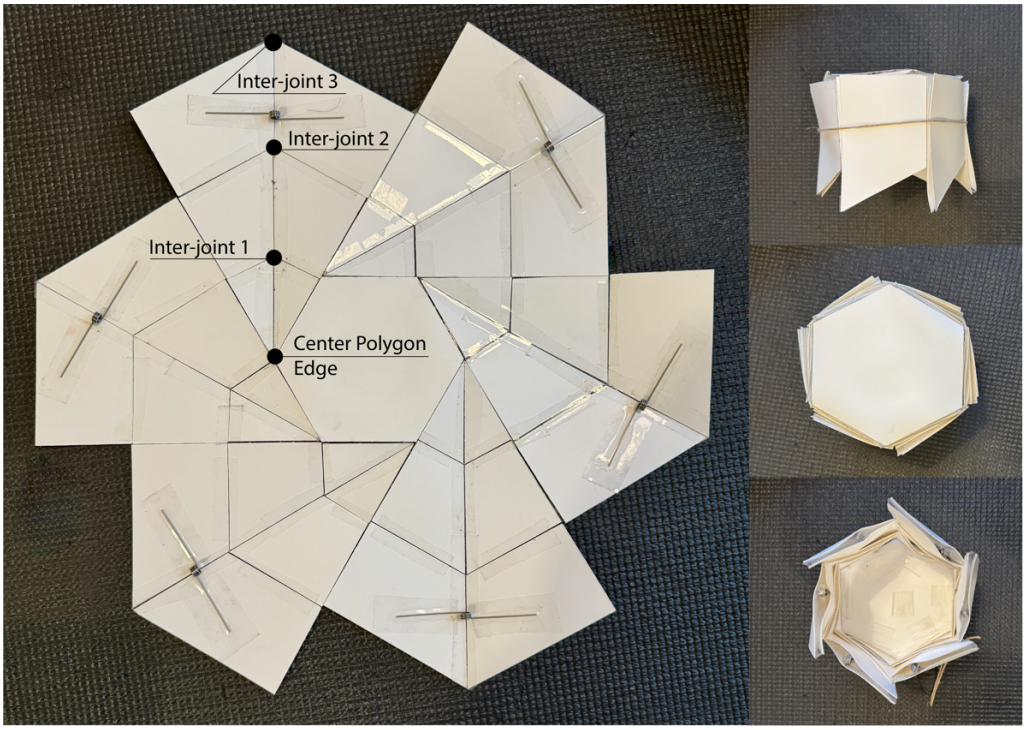

Figure 4.2. The experimental model in deployed and compact form.

First, the flasher was manually compressed until $\theta = \pi$, and held together with twine. The twine was manually cut from a distance and the flasher was allowed to automatically deploy until movement ceased. Two models were made: the first, a "nonfixed model", allowed the center polygon complete freedom in movement along the (x, y) directions on the plexiglass surface. The second "fixed model" used duct tape to keep the center polygon edges adhered to the plexiglass surface and allowed only the panels free movement. Keeping the center polygon fixed in this way constrains the center polygon's rotational movement and negates any potential frictional effects.

Video analysis was completed using Vernier Video Analysis software. Due to the symmetric properties of the flasher, it is sufficient to isolate one panel in addition to the center polygon for analysis. The origin for both the cartesian (x, y) and polar (r, θ) coordinates is set as the center of the flasher in its compressed form prior to deployment. During deployment, as the center polygon was not fixed, the non-fixed model translated in the (x, y) direction a total of (0.0719 m, 0.168m). This arises from many intricate factors, an obvious one of which is the timing of the torsional spring deployment: which will not be explored in this research due to its complexity. The dominant factor is the light mass of the model due to the use of Yupo paper, which has a low density of 0.8 $\frac{g}{m^2}$.

Figures 4.3 and 4.4 shows the trajectory of each joint in the (x, y) cartesian plane with respect to time for both the non-fixed and fixed models. Note that for the fixed model, the center polygon edge is not considered as its displacement is assumed to be zero.

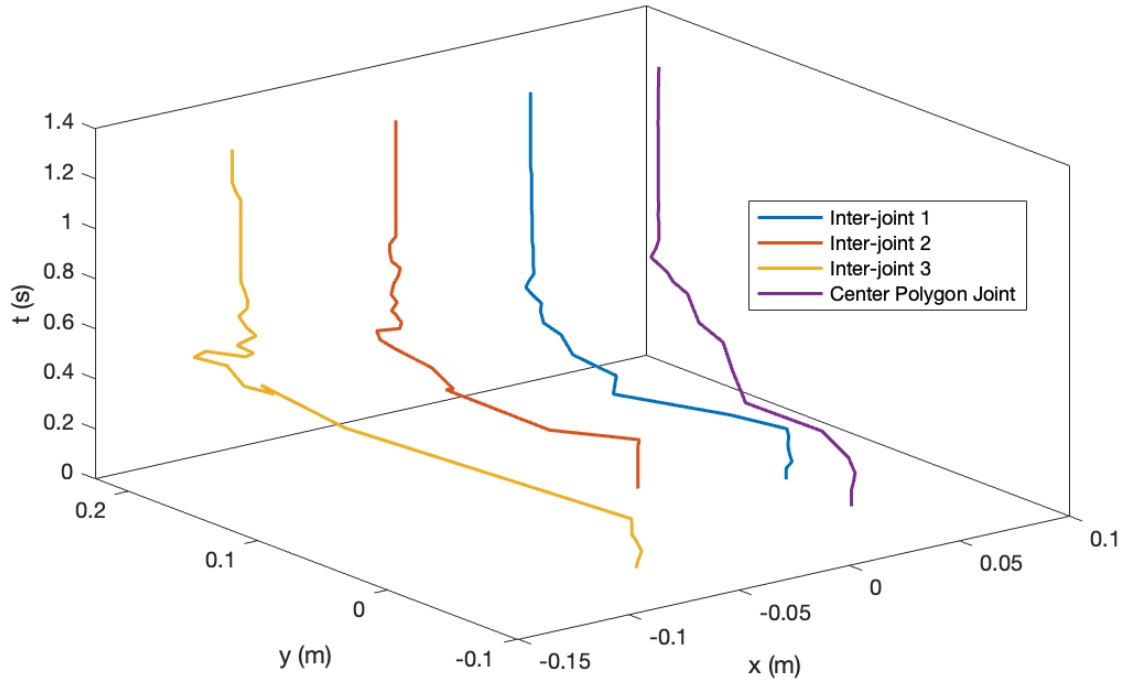

Figure 4.3. Trajectory of the non-fixed model's inter-joints in the (*x, y*) plane.

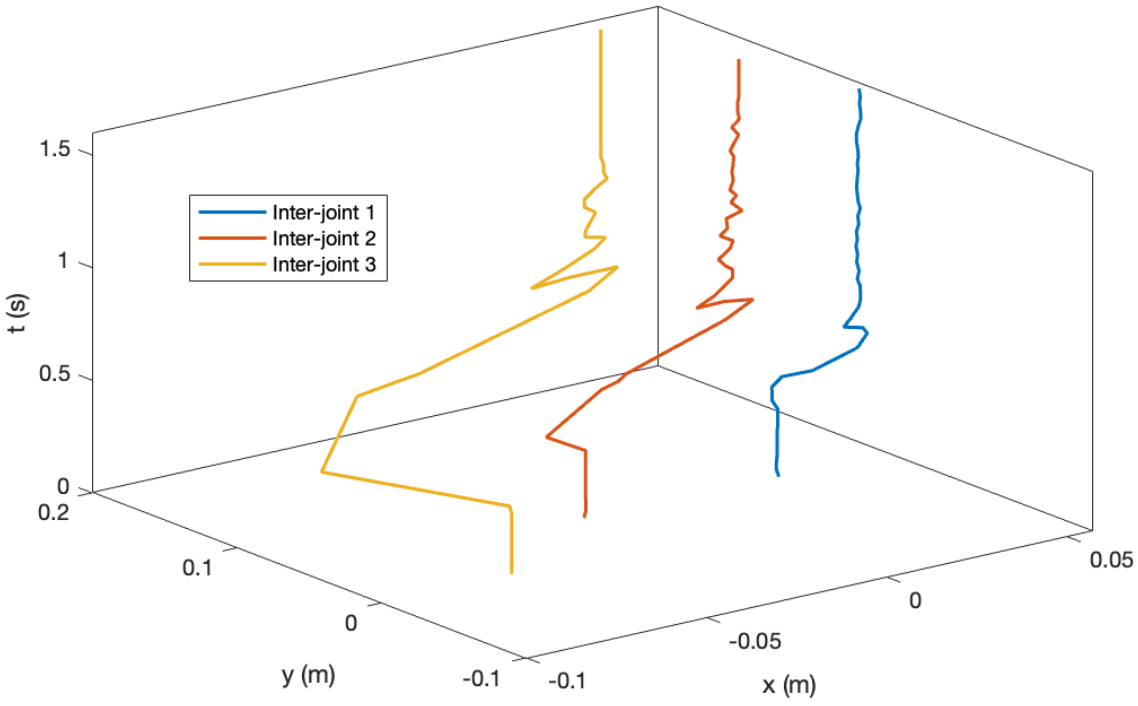

Figure 4.4. Trajectory of the fixed model's inter-joints in the (*x, y*) plane.

Analysis of joint trajectory shows that the non-fixed model appeared to be more stable during and after deployment. While oscillations before settling into their final position occurred among all its three inter-joints, they were not as large in displacement and temporal magnitude as those seen in the fixed model. These oscillations are due to the damping effects arising from the use of Yupo and torsional springs. As Yupo is extremely flexible and lightweight, the distribution of internal forces after deployment causes intense movement. Additionally, the torsional springs are adhered to the Yupo panels and add to the damping effects.

The damping effects are strongest at Inter-joint 3 and are most evident after the initial stages of deployment when the mountain and valley crease folds approach stability to lie near flat against the plexiglass surface. Isolating the inter-joints of the two models and treating each as an underdamped oscillator, an experimental damping ratio and experimental damping coefficient for each can be calculated as shown in equations 12-16. r_3 represents the distance vector of inter-joint 3, X_1, X_2 the largest amplitudes of the vibration at times Y_1, Y_2, ω_d the damped frequency, ω_n the natural frequency, ζ_c the calculated damping ratio, and c_c the calculated damping coefficient. The facet creases of the two subunits at $h = 3$ as explained before are intra-joints modeled via a hinge mechanism and so the relationship for springs in series is applied to find an equivalent stiffness factor K_{eq} for inter-joint 3. For inter-joints 1 and 2, the spring is removed from the series. *m* represents the combined mass of both subunits. Table 4-2 shows the $\zeta_c, \omega_n, \mathrm{c}_c$ for each inter-joint.

$$t = Y_2 - Y_1 \quad (12)$$

$$\frac{X_1}{X_2} = e^{\zeta_c \omega_n t} \quad (13)$$

$$\omega_d = \frac{2\pi}{t} = \omega_n \sqrt{1 - \zeta_c^2} \rightarrow \omega_d^2 = \omega_n^2 - \zeta_c^2 \omega_n^2 \quad (14)$$

$$\frac{1}{K_{eq,\ subunut\ h}} = \frac{1}{K_f} + \frac{1}{K_S} + \frac{1}{K_f} \text{ or } \frac{1}{K_{eq}} = \frac{1}{K_f} + \frac{1}{K_f} \quad (15)$$

$$c_c = 2\zeta_c \sqrt{m K_{eq}} \quad (16)$$

Table 4-2. The ω_n, ζ_c, c_c values for both models.

	Fixed Model			Non-fixed Model		
	Inter-joint 1	Inter-joint 2	Inter-joint 3	Inter-joint 1	Inter-joint 2	Inter-joint 3
$\omega_n \left(\frac{\theta}{s}\right)$	37.7085	37.7076	37.7754	47.4813	47.4846	47.4935
ζ_c	0.009754	0.006949	0.005993	0.001622	0.01192	0.02280
c_c	0.0001229	0.0001523	0.00009111	0.00002044	0.0002612	0.0003466

The two models experienced drastically different patterns concerning damping effects among their inter-joints. For the fixed model, distance from the center polygon is negatively correlated to the damping ratio and damping coefficients. In contrast, the correlation appears to be positive within the non-fixed model. The effect of distance on the damping ratio is more dominant for the non-fixed model as demonstrated by its larger magnitude in the slope of its $\zeta_c\ vs. r$ function in Figure 4.5. While ζ_c decreased from inter-joint 1 to inter-joint 3 in the fixed model, the difference is not as pronounced as in the non-fixed model. This could be indicative of a constant ζ_c along inter-joints for fixed models and that the negative correlation found through analysis due to external factors.

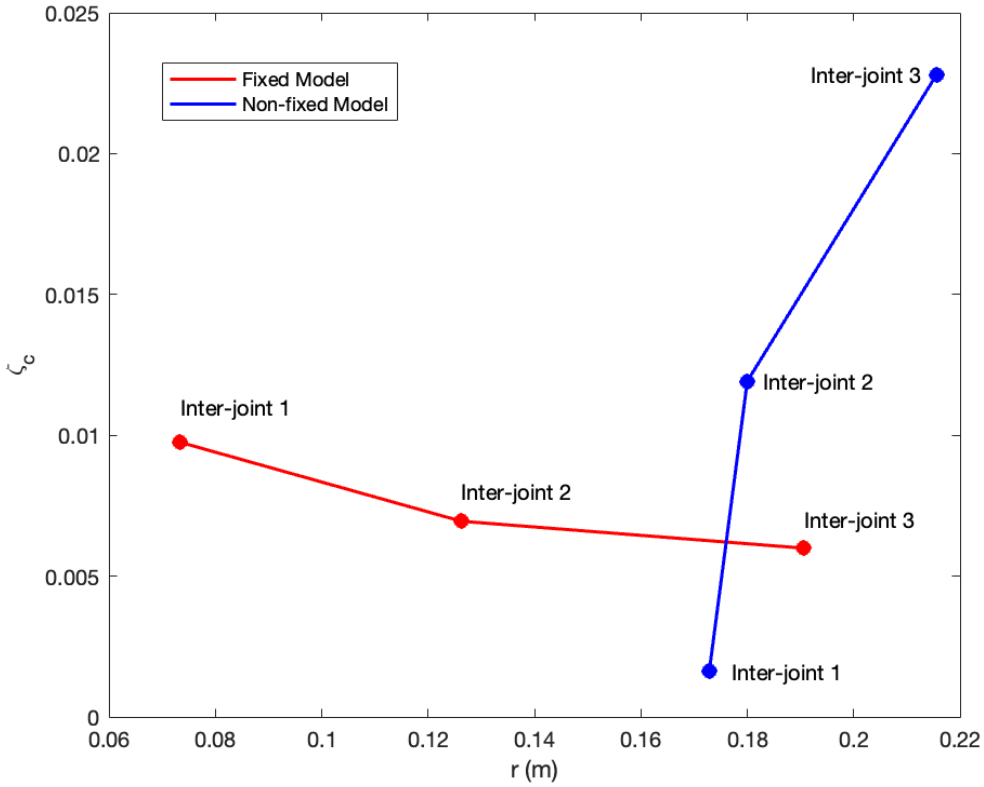

Figure 4.5. $\zeta_c \; vs. \; r$ for the inter-joints of both models.

Alongside damping, analysis of the torque experienced by each joint is also important for design considerations. It is an example of an internal constraint force and helps to model overall force distribution within the model. To calculate the torque experienced at each inter-joint, the moment of inertia and angular acceleration for each must be calculated. The angular acceleration was extrapolated from the angular velocity collected during video data analysis. The moments of inertia were found through treating the panels as point masses concentrated at each inter-joint rotating about the origin and so $\tau = I\alpha = mr^2\alpha$. Figure 4.6 shows the angular velocity and torque experienced by each inter-joint for both models as a function of time.

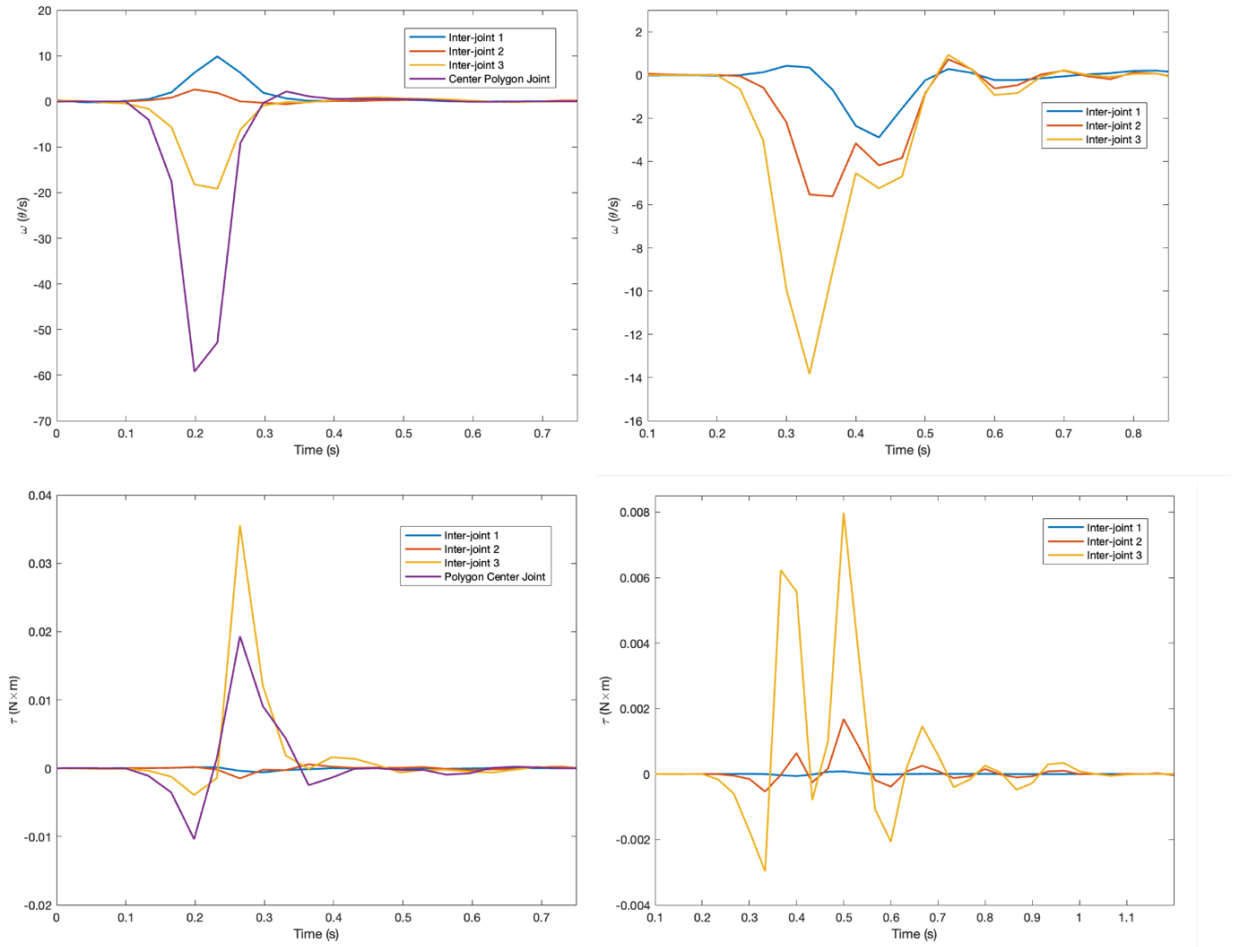

Figure 4.6. $\omega\ vs.\ t$ and $\tau\ vs.\ t$ for the non-fixed (left) and fixed (right) models.

Between the two models, there are some basic similarities. First, distance from the center polygon and the magnitude τ, ω are positively correlated across all inter-joints for both models. Second, the τ, ω functions adapt a sinusoidal form which can be attributed to the damping effects discussed previously.

Of greater interest is the differences seen between the models. The range of torque and angular velocity are smaller in magnitude for the fixed model than for the non-fixed model. This may be because the non-fixed model, free to translate, shifted and rotated in a

way the fixed model did not experience and had more irregularity during its deployment. As the angular velocity was calculated using the polar coordinate data in the form (r, θ), the translation amplified the values for τ, ω, and also meant that inter-joint 1, inter-joint 2, and the center polygon edge joint were able to experience non-negative angular velocity (embodied by counterclockwise rotation).

Additionally, the inter-joints of the fixed model experienced a larger magnitude of reaction torque than the non-fixed model. Deployment was complete near t = 0.4 s, but each inter-joint experienced an intense rebound effect as shown by the sinusoidal forms that their τ, ω functions adopt. Close analysis of the τ function for inter-joint 3 of the fixed model suggests a positive correlation between distance from the center polygon and the magnitude and duration of reaction torque. While the non-fixed model also experienced reaction torque, its effect was greatly reduced.

Discussion

A mathematical relationship of geometric parameters affecting $R_{Deployment}$ of flasher patterns served to establish an $n = 6, h = 3$ template for both the dynamic and experimental models. The mathematical model was simplified as extensive research has been done concerning zero-thickness flasher patterns. For future research, it may serve as useful to explore the performance of flashers with curved creases and circular panels. The most common existing zero-thickness and finite-thickness flasher pattern models use non-curved folds as they allow for easy mathematical analysis but in doing so, limit real-world flasher adaptations.

Next, combining the mechanical and material properties for the flasher led to the creation of an insightful dynamic model which holds great potential for future use. Its visualization of fold geometry and strain distribution allows for analysis of a flasher's individual structural components during the deployment process and highlights areas where reinforcement against high strain and internal forces may be necessary. Additionally, the model incorporates material properties via a "stiffness" matrix whose entries can easily be found for most flasher pattern geometries and known material values: giving it great potential to be applied across various disciplines. To improve on the accuracy of the model, future research on the incorporation of other properties such as frictional effects arising from subunit interactions would be useful.

Finally, Yupo paper served as a useful medium for the creation of an experimental model. While Yupo served as an adequate material for this stored-energy-based deployable flasher model, analysis of its performance suggests that the ideal material should be denser

to allow for more mass to limit unwanted model movement during deployment. Yupo's flexibility and durability were its largest strengths and the manufacturing processes that give rise to its properties could be useful for developing future materials for use in flasher-inspired products or designs that require fast and unstable movement.

The insertion of torsional springs at important inter-joints for stored energy to be used for automatic deployment proved effective and through manipulating torsional angle, stiffness, or other parameters, one can control the speed and quantity of deployment. The rigidity of the springs may have increased the damping effects and exploration on using elastic materials, different hinge/joint mechanisms, etc. at inter-joints or other locations of kinematic importance would be beneficial. Wang et al. [15] found great success when utilizing rubber bands modeled as linear springs for automatic deployment when creating a thick, curved-surface flasher.

Building upon knowledge gained from the dynamic model, video analysis was useful in investigating the damping effects, angular motion, and torque distribution among the experimental model's inter-joints. Between the fixed and non-fixed models there appears to be a trade-off between damping and the torque experienced: if the aim is to limit damping effects, the fixed model is a better fit as through limiting the rotational movement of the center polygon, the ζ_c values felt within the panels' inter-joints decreases. However, it also increases the instability of the inter-joints' torque values. The non-fixed model's angular movement and torque distribution was more stable, but it experienced larger damping effects and a larger magnitude of torque. Additionally, as the center polygon was not fixed to the plexiglass surface and free to rotate and translate, the model shifted during deployment. This may be due to the use of torsional springs and their complex deployment

timing and the light mass of the model. If one were to use a material with a larger mass, it would stabilize the transformation of the potential energy stored within the springs to kinetic energy during deployment and limit overall translation.

Another potential to lower torque comes from increasing the flasher order. As the order increases, the (r, θ) displacement for each inter-joint decreases. Combined with the fact that there are more inter-joints across the model, the torque concentrated at each inter-joint would decrease. Similarly to increasing the order of the flasher, increasing its height parameter could stabilize and lower the torque reaction. Increasing the height may also increase damping effects as shown by inter-joint 3 (with the largest mass and $A_{subunit}$), having the largest ω_n, ζ_c, c_c values in the non-fixed model.

Conclusion

A mathematical exploration of the origami flasher design was used to identify $n = 6, h = 3$ as the optimal parameters for a high $R_{Deployment}$ and an effective experimental model. Next, the mechanical and material properties of the flasher were combined as a system of linear equilibria solved using finite element analysis to create a dynamic model used to visualize folding behavior and strain distribution. Finally, an experimental strain-energy-based deployable model was made using Yupo paper and video analysis done to understand damping behavior, angular motion, and torque distribution. The results show that while Yupo material is not ideal for flasher-based designs, its flexibility and durability properties show promise for adaptation of other materials. Additionally, the dynamic model created through software holds potential to be used in many applications. Finally, further research into the impact of flasher geometry such as order and height on the torque distribution could serve useful for product design.

References

[1] Zhang, P., Liu, X., Liu, P. et al. (2020). Capturing transient antibody conformations with DNA origami epitopes. *Nature Communications 11*, 3114. https://doi.org/10.1038/s41467-020-16949-4.

[2] Shafer, J. (2001). Origami to Astonish and Amuse, St. Martin's Griffin, New York.

[3] Hoberman, C. (2010). Folding Structures Made of Thick Hinged Sheets. U.S. Patent No. 7,794,01914.

[4] Trautz, M., & Kunstler, A. (2010). Deployable folded plate structures – folding patterns based on 4-fold mechanism using stiff plates. *Editorial Universitat Politècnica de València*. http://hdl.handle.net/10251/7278.

[5] Tachi, T. (2011). Rigid-Foldable Thick Origami. Origami 5, CRC Press, Boca Raton, FL, p. 253–264. 10.1201/b10971-24.

[6] Bhuiyan, Emran Hossein. (2017). Dynamic Modeling and Analysis of Strain Energy Deployment of an Origami Flasher. *The University of Toledo*, 42-67.

[7] Zirbel, S. A., Lang, R. J., Thomson, M. W., Sigel, D. A., Walkemeyer, P. E., Trease, B. P., Magleby, S. P., and Howell, L. L. (2013). Accommodating Thickness in Origami-Based Deployable Arrays. ASME *Journal of Mechanical Design 135(11)* pp. 2-9. 111005.

[8] Tang, Y., Liu, J., Wu C., & Zhao, P. (2016). Configuration design and crease topology of origami-inspired spinning space deployable structures. *Proceedings of the Institution of Mechanical Engineers, Part C: Journal of Mechanical Engineering Science.* pp. 6-7. 10.1177/09544062231207541.

[9] Schenk, M., & Guest, Simon D. Origami folding: a structural engineering approach." *In Origami 5*, edited by Patsy Wang-Iverson, Robert J Lang, and Mark Yim, pp. 293-305. CRC Press, 2011.

[10] Garza, L.R. (1966). A Comparison of Flexible and Rigid Ring Baffles for Slosh Suspension. *George C. Marshall Space Flight Center NASA*. NAS8-20290(1). 1-6175-00010.

[11] Troise, Andrea. (2023). Reduced-order modelling of the deployment of a modified flasher origami for aerospace applications. *Aeronautics and Astronautics – AIDAA CCVII International Congress, Materials Research Proceedings 27(2023)* pp. 547-552. 10.21741/9781644902813-120.

[12] Ghassaei, A., Demaine, E., & Gershenfeld, N. (2018). Fast, Interactive Origami Simulation using GPU Computation. *Center for Bits and Atoms, Massachusetts Institute of Technology.*

[13] Zhu, Y., & Filipov, E. (2021). Sequentially Working Origami Multi-Physics Simulator (SWOMPS): A Versatile Implementation. *ASME 2021 International Design Engineering Technical Conferences and Computers and Information in Engineering* Conference. 10.115/DETC2021-68042.

[14] Budynas, R.G. & Nisbett, J. K. (2015). *Shingley's Mechanical Engineering Design*. 10th Edition. 124.

[15] S. Wang, Y.H Gao, H.L Huang, et al. (2022). Design of deployable curved-surface origami flashers. *Mechanism and Machine Theory,* pp. 167-169: 104512.